Supporting Information

for "Tailoring Kinetics on a Topological Insulator Surface by Defect-Induced Strain: Pb Mobility on Bi_2Te_3"

Wen-Kai Huang,[†] Kai-Wen Zhang,[†] Chao-Long Yang,[†] Haifeng Ding,[†,‡] Xiangang Wan,[†,‡] Shao-Chun Li,[†,‡]*

[†]National Laboratory of Solid State Microstructures, School of Physics, Nanjing University, Nanjing 210093, P. R. China, [‡]Collaborative Innovation Center of Advanced Microstructures, Nanjing University, Nanjing 210093, P. R. China

James W. Evans,[§,‖] and Yong Han[§,‖,*]

[§]Department of Physics and Astronomy, Iowa State University, Ames, Iowa 50011, United States, [‖]Ames Laboratory—U. S. Department of Energy, Iowa State University, Ames, Iowa 50011, United States

*Address correspondence to

S.-C.L.
Email: scli@nju.edu.cn; Tel: +86-(0)25-83596050

Y.H.
Email: yong@ameslab.gov; Tel: 515-294-4819

Crystal structure of Bi_2Te_3

Bulk Bi_2Te_3 has a rhombohedral primitive cell, which contains two Bi and three Te atoms, as indicated in Figure S1. The experimental values [1] of the four independent lattice parameters defining the primitive cell are: (111) surface lattice constant $a = 0.4386$ nm, long diagonal distance $c = 3.0497$ nm, internal coordinates $u = 0.4000$ for Bi and $v = 0.2095$ for Te. Along the [111] direction, i.e., c-axis, the crystal is repeatedly stacked by quintuple layers (QLs), see Figure S1a for the symmetric geometry. Other useful lattice constants deriving from the above four independent lattice parameters are indicated in Figure S1, and all experimental values are listed in Table S1.

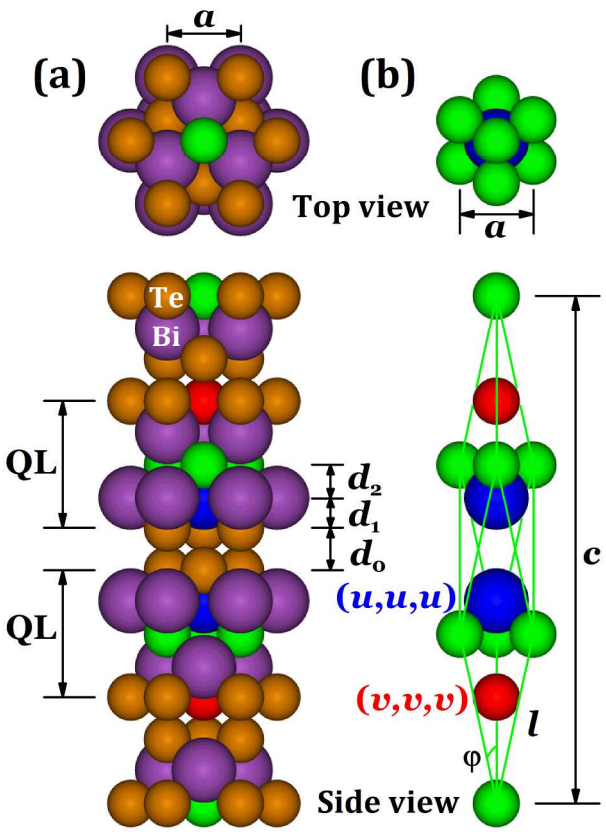

Figure S1 Crystal structure of Bi_2Te_3. Small and big spheres represent Te and Bi atoms, respectively. (a) A hexagonal cell showing the QLs and interlayer spacings, d_0, d_1 and d_2. (b) A rhombohedral primitive cell containing five atoms symmetrically: two Bi atoms (blue), two Te atoms (red), and eight Te atoms (green) on vertices of the rhombohedron contribute one Te atom to the cell. Note that the primitive cell in (b) is contained in the hexagonal cell in (a), as indicated by the colors of atoms for clarity. The top view on the upper panel shows the (111) surface structure.

Table S1. Lattice constants (illustrated in Figure S1) of bulk Bi_2Te_3 obtained from different functionals in DFT analysis and from experiments.

Lattice constants	PBE	PBE+optB86b	PBE+SOC	PBE+opt86b+SOC	Experiments [1]
a [nm]	0.4445	**0.4405**	0.4461	0.4537	0.4386
c [nm]	3.1379	**3.0616**	3.0821	3.4138	3.0497
l [nm]	1.0770	**1.0517**	1.0591	1.1677	1.0476
φ	23.817°	**24.174°**	24.317°	22.402°	24.166°
d_0 [nm]	0.2927	**0.2663**	0.2693	0.3750	0.2613
d_1 [nm]	0.1722	**0.1737**	0.1740	0.1721	0.1743
d_2 [nm]	0.2045	**0.2034**	0.2051	0.2093	0.2033
u	0.3985	**0.3998**	0.3999	0.3947	0.4000
v	0.2133	**0.2102**	0.2103	0.2216	0.2095

Experimental information

Below we show additional STM images of surface structures relevant to our study. Figure S2 show in greater detail a point-like defect on the Bi_2Te_3(111) film clearly indicating the strain (stretching) of the surface atoms. Figure S3 shows surface and subsurface domain boundaries in a thin Bi_2Te_3(111) film grown on a Si(111)-7×7 substrate. It is possible that defects could be associated with not just low-angle tilt boundaries, as discussed in the text, but also with subsurface domain boundaries. Figure S4 illustrates a fast Fourier transform (FFT) analysis and strain field maps from a geometric phase analysis (GPA) of an STM image for a strained surface area. Figure S5 shows a variety of defective morphologies of Bi_2Te_3(111) films obtained by tuning growth kinetics. Figure S6 illustrates scanning tunneling spectroscopy (STS) data for strained and unstrained surface regions. Figures S7 and S8 provide additional images of the surface morphology after depositing a small amount of Pb. Figure S9 shows sequential STM images for hopping of a Pb adatom.

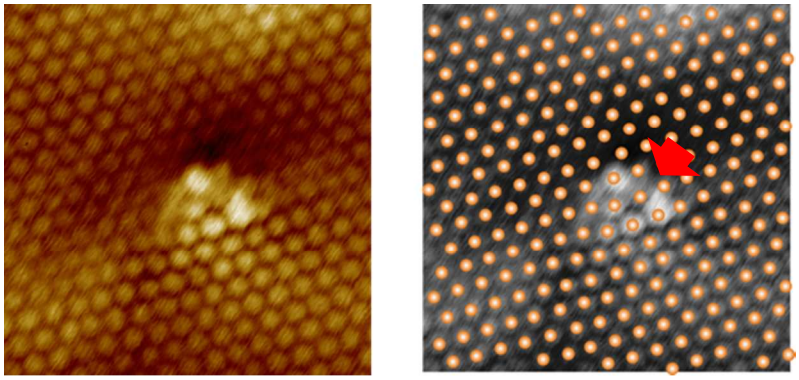

Figure S2 A point-like defect with atomic resolution, and the corresponding lateral stretch of lattice atoms. The red arrow marks the position of the defect center.

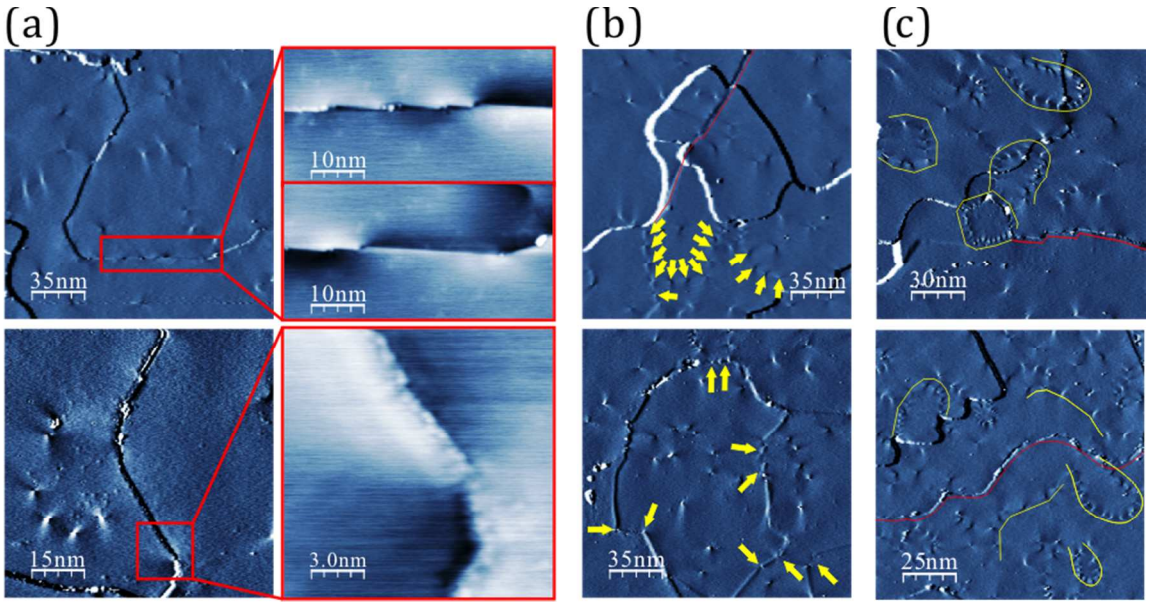

Figure S3 (a) Left panel: large scale derivative STM images (tunneling current I = 0.1 nA, bias voltage U = +1.0 V) showing the surface domain boundary. Image size: 175×175 nm^2 (up) and 75×75 nm^2 (down). For the top left image, a zoom-in of the left (right) half of the red rectangle are shown in the top (bottom) right panel. For the bottom left image, a zoom-in of the red square is shown in the right panel. (b) Derivative STM images (I = 0.1 nA, U = +1.0 V) showing the subsurface domain boundary, and the point-like defect formed along the domain boundary. Positions of point-like defects are marked by yellow arrows. The red curve traces the surface domain boundary from the lower terrace to the upper terrace where it becomes a subsurface domain boundary. (c) Derivative STM images showing the traces of point-like defects (by yellow lines) and surface domain boundaries (by red lines).

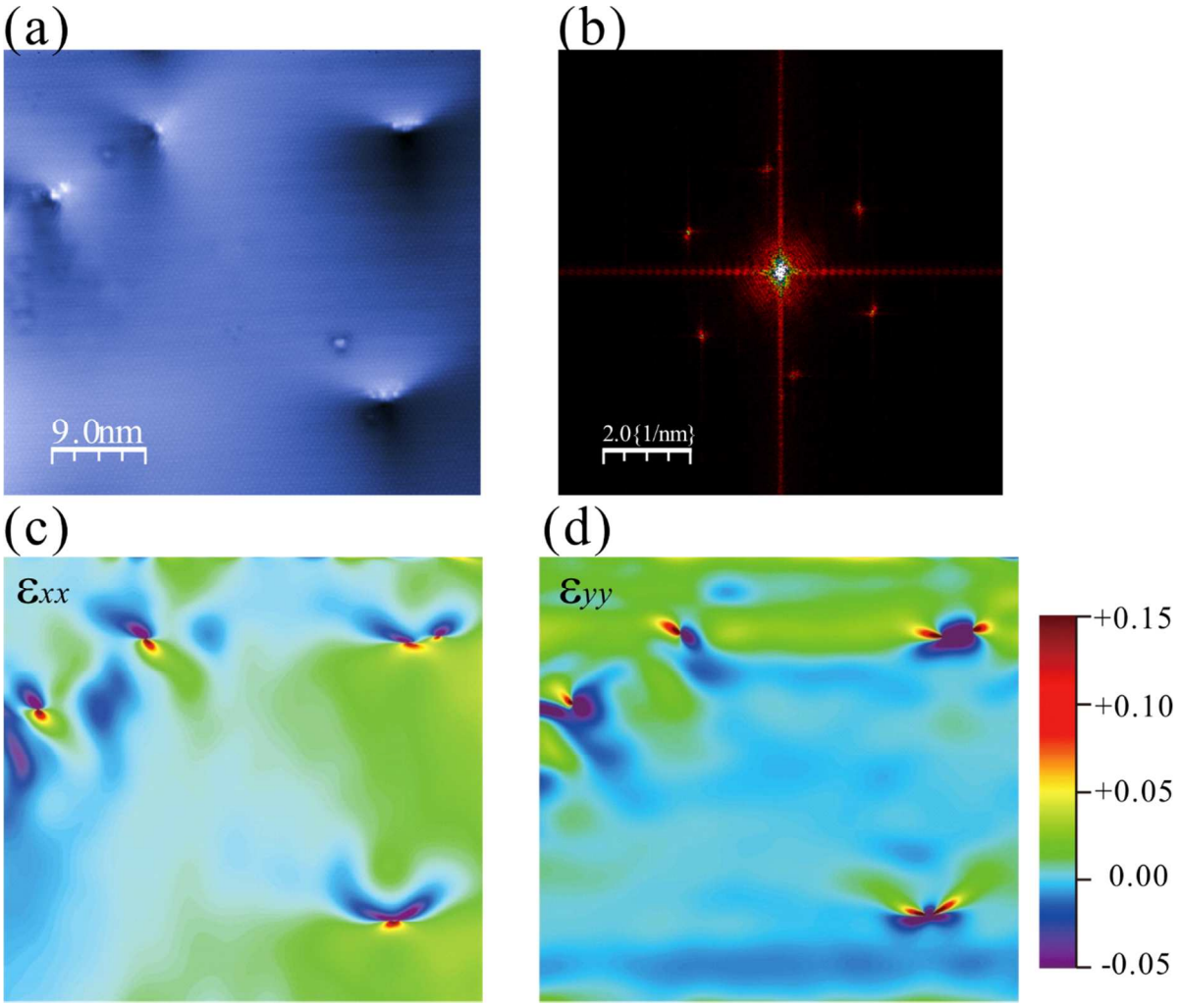

Figure S4 (a) STM image of 42×42 nm². (b) The fast Fourier transform (FFT) of image (a). (c) ε_{xx} and (d) ε_{yy} strain map obtained via the geometric phase analysis (GPA) of image (a). Positive (negative) values correspond to tensile (compressive) strain.

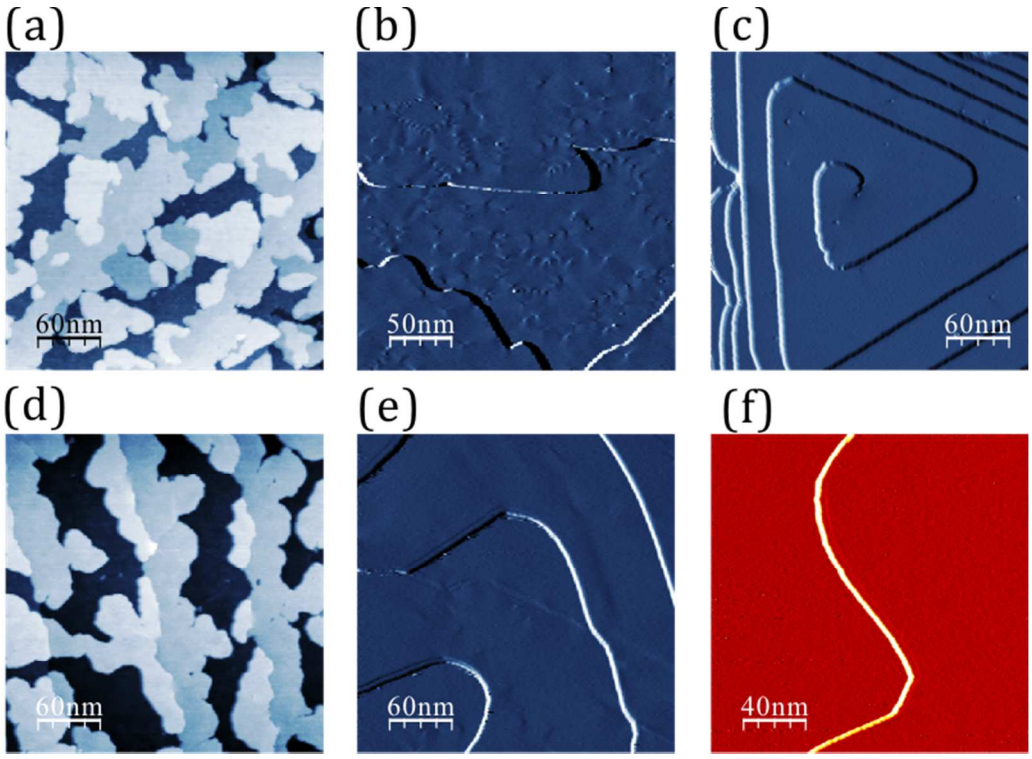

Figure S5 (a) Bi_2Te_3 film with the thickness of ~3 QLs grown on Si(111). Deposition rate: ~ 0.5 ML/min; image size: 300×300 nm^2. (b) Bi_2Te_3 film (derivative STM image) with the thickness of ~10 QLs grown on Si(111). Deposition rate: ~ 0.5 ML/min; image size: 250×250 nm^2. (c) Bi_2Te_3 film (derivative STM image) with the thickness of ~30 QLs spirally grown on Si(111). Deposition rate: ~ 0.5 ML/min; image size: 250×250 nm^2. (d) Bi_2Te_3 film with the thickness of ~3 QLs grown on Si(111). Deposition rate: ~ 0.05 ML/min; image size: 300×300 nm^2. (e) Bi_2Te_3 film (derivative STM image) with the thickness of ~10 QLs grown on Si(111). Deposition rate: ~ 0.05 ML/min; image size: 300×300 nm^2. (f) Bi_2Te_3 film (derivative STM image) with the thickness of ~10 QLs grown on $NbSe_2$ substrate. Deposition rate: ~ 0.05 ML/min; image size: 250×250 nm^2. For all images, tunneling current I = 0.1 nA, and bias voltage U = +1.0 V.

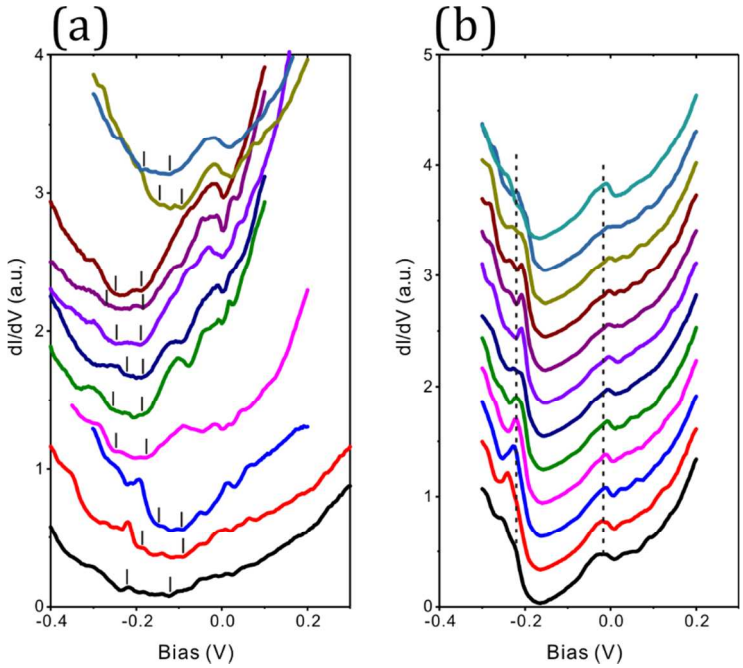

Figure S6 (a) STS measured near 11 point-like defects at 4 K. The gap is indicated by black vertical lines. (b) STS measured along a line of 30 nm in the unstrained surface region at 4 K. Two dotted lines indicate the edges of valence band and conductance band.

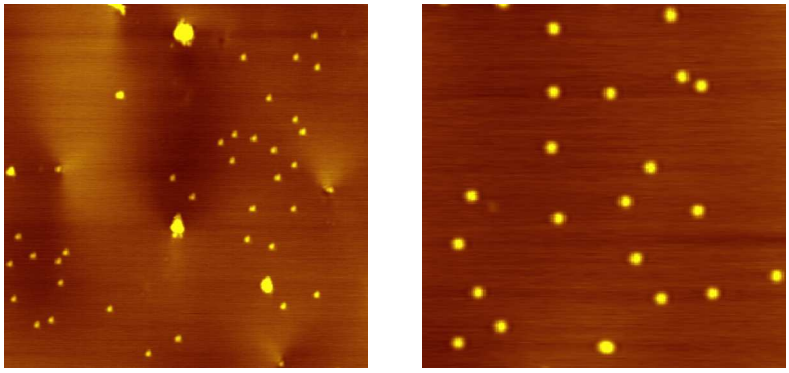

Figure S7 The surface morphology after depositing small amount of Pb (coverage: 0.003ML. Image sizes: 50×50 nm^2 (left); 25×25 nm^2 (right).

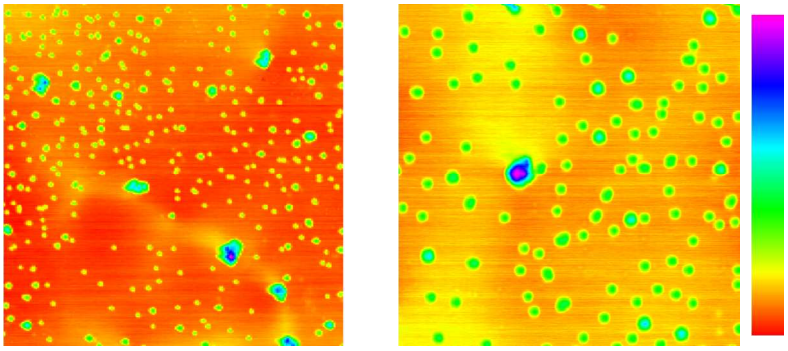

Figure S8 The surface morphology after depositing small amount of Pb (coverage: 0.015ML. Image sizes: 100×100 nm^2 (left); 40×40 nm^2 (right). Morphology heights (color bar): red (low); pink (high).

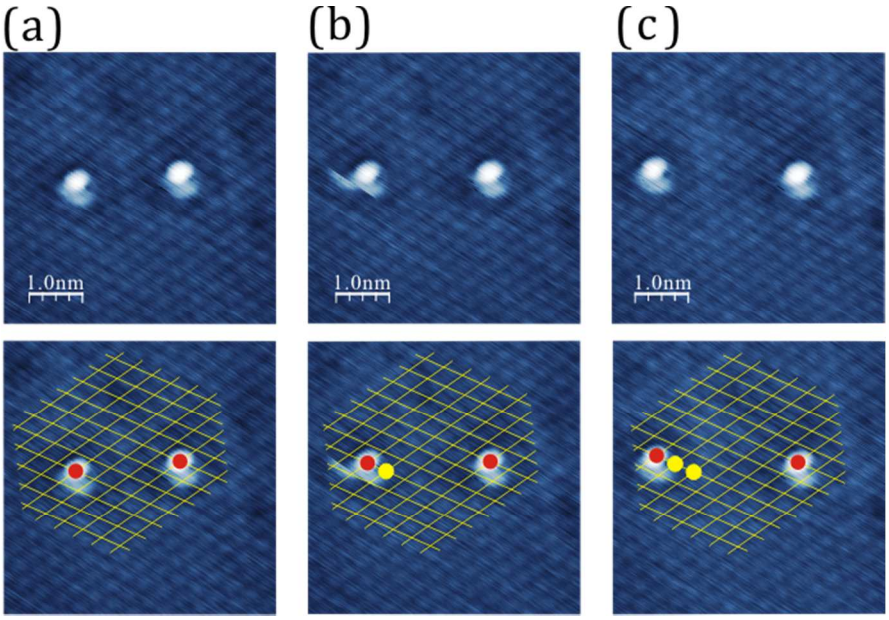

Figure S9 Sequential STM images collected at the same area, showing the hopping of a Pb adatom (the left one in the image) at liquid-N_2 temperature. The time interval for taking each image is about 5 min. Image size is 5×5 nm^2. Tunneling current I = 0.1 nA, and bias voltage U = +1.0 V. The lower panel corresponds to the same images as the upper panel, but it is overlaid with marks indicating the location of single Pb adatoms (red dots) and of the substrate lattice (yellow lines). (a) Red dots indicate the initial positions of two Pb single adatoms. (b, c) Red dots indicate the current positions of Pb adatoms. Yellow dots indicate the previous positions before hopping.

Density functional theory (DFT) calculation details

In this work, total energies are calculated from DFT by running the plane-wave VASP code [2-5]. We use the projector augmented wave (PAW) method [6, 7] for the electron-core interactions, and the Perdew-Burke-Ernzerhof (PBE) generalized gradient approximation (GGA) [8] for exchange and correlation. The corresponding pseudopotentials newly released in 2013 are generated by the VASP group. The energy cutoffs for the plane wave basis are set to be the VASP default value 242.8 eV, which was tested to be enough for energy convergence. For the accuracy of energy minimization, the magnitude of the force acting on each atom to be allowed to relax is less than 0.1 eV/nm. Selection of supercell size and the corresponding Γ-centered **k** meshes are always tested carefully for energy convergence. For surface calculations, the vacuum thickness between the slab and its nearest neighboring replica is taken to be 2 nm. We also examine the effects of van der Waals (vdW) interactions and spin-orbital coupling (SOC), and consequently choose an appropriate functional for calculating adsorption energies (E_{ad}) and diffusion barriers (E_{d}) of Pb on Bi_2Te_3(111). E_{d} values are obtained from minimum energy paths (MEPs) determined from the climbing nudged elastic band (cNEB) method [9, 10].

In previous DFT calculations for Bi_2Te_3, the effects of vdW interactions and SOC on lattice parameters have been discussed [11, 12]. In this work, we choose the optB86b-vdW functional [13], which can well reproduce the experimental lattice constants and interlayer spacings [12]. In Table S1, we listed our results from different functionals in our DFT analysis and from experiments. As seen in Table S1, the lattice constants from PBE+optB86b-vdW are closest to experimental values, therefore taken in our calculations for surface. In the above calculations for lattice constants of bulk Bi_2Te_3, we use the primitive cell in Figure S1b, with **k** meshes not less than 7×7×7 until enough convergence accuracy is reached.

To assess E_{d} for Pb adatoms on Bi_2Te_3(111), we first determine the optimized local adsorption site configurations by relaxing Pb in the fcc and hcp site regions. Using these as the two endpoints, we perform the cNEB calculations to obtain the corresponding MEPs, for diffusive hopping between these sites. The hopping barrier, E_{d}, is determined from the difference between the energy at the transition state (TS), which is a saddle point in the potential surface energy (PES) for Pb adsorption, and the energy at the most stable fcc adsorption site. Here it is should be mentioned that the energy after a swapping a Pb adatom with a nearest neighboring Te atom on surface is much higher than the energy at the TS for hopping. This indicates that the two-atom exchange mechanism [20] is extremely unfavorable and therefore the *hopping* barrier corresponds to the activation energy, E_{d}, for long-range surface diffusion.

As an aside, we have assessed how E_{d} depends on slab thickness, using a 3×3 supercell with a **k** mesh of 5×5×1. We obtain $E_{\mathrm{d}} = 0.228$ and 0.233 eV for 1- and 2-QL unstrained Bi_2Te_3(111) as substrate, respectively. The small change (only 5 meV) of E_{d} means that a 2-QL slab is thick enough for calculating E_{d}, despite the fact that the energy band structure has noticeable thickness-dependence for thin TI films (up to few QLs) [14-19]. Thus, in our calculations for Pb diffusion on a strained surface, we always use a 2-QL slab as substrate with the bottom 1 QL fixed during relaxation (note that only bottommost 1-ML Te is fixed in the above calculation for 1-QL slab).

In addition, we also tested the effects of SOC on the adsorption energy and diffusion barrier of Pb on 1-QL unstrained slab; for this case, we found that the change in both ΔE_{ad} and E_{d} due to SOC is only a tiny value of ~6 meV, and therefore we do not include SOC in the above strained-surface calculations.

Bifurcation in the location of the most stable adsorption site with varying strain

As noted in the text and shown explicitly in the inset to Figure 3d, detailed DFT analysis reveals a bifurcation or sudden jump in the location of the most stable adsorption site in the fcc region. For $\varepsilon > \varepsilon_{\mathrm{c}}$ (tensile strain), this stable site is close to the high-symmetry fcc site. However, as ε drops below ε_{c} (including the regime of compressive strain), the stable site jumps to a location closer to the bridge site, while the stable site in the hcp region is close to the high-symmetry hcp site except the larger compressive $\varepsilon < \sim -1\%$. See the inset in Figure 3d. As noted in the text, this behavior can be traced to a seesaw-type bifurcation in the shape of PES for Pb adatom binding along a line through the high-symmetry fcc, bridge, and hcp sites. A more complete set of PES profiles capturing this behavior is shown in Figure S10. These images also show behavior when substrate atoms are frozen in which case the bifurcation does not occur.

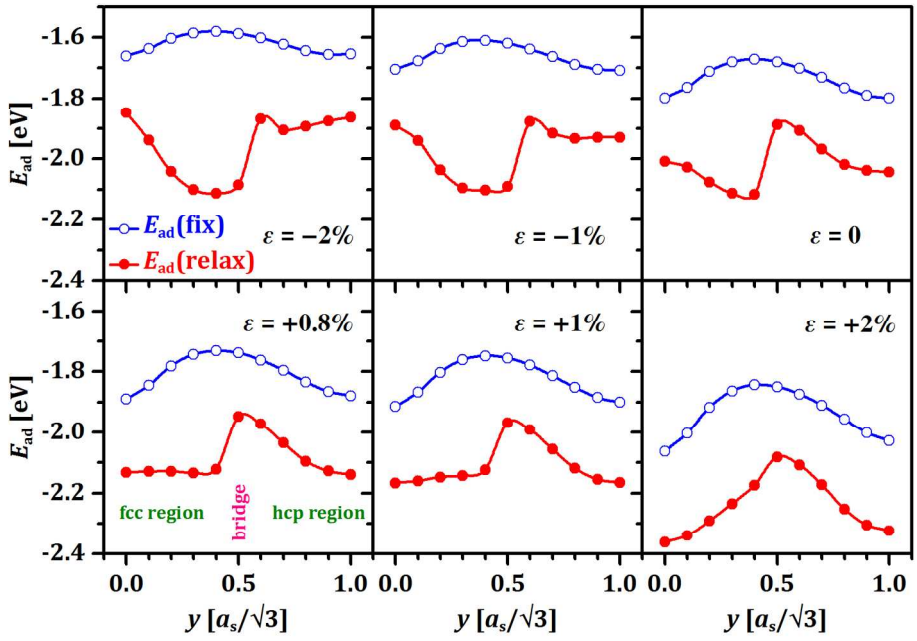

Figure S10 PES of Pb adatom binding along a line (at $x = 0$) through the high-symmetry fcc, bridge, and hcp sites for different ε. The origin of x and y coordinates is chosen at the high-symmetry fcc site, see the inset of Figure 3a. The unit $a_{\mathrm{s}}/\sqrt{3}$ of location y is the distance between high-symmetry fcc and hcp sites. The dots on red curves are obtained by equidistantly varying y (fixed) but fully relaxing x and z coordinates of Pb adatom as well as all top-QL atoms of the substrate. The circles on blue curves are obtained by equidistantly varying y (fixed) and only relaxing z coordinate of Pb adatom without substrate relaxation. Each curve is generated from a modified Bézier method [21] by individually fitting eleven equidistant DFT data points (dots or circles) from high-symmetry fcc site to hcp site along the y direction.

References

1) Nakajima, S. *J. Phys. Chem. Solids* **1963**, *24*, 479.

2) Kresse, G.; Hafner, J. *Phys. Rev. B* **1993**, *47,* 558.

3) Kresse, G.; Hafner, J. *Phys. Rev. B* **1994**, *49,* 14251.

4) Kresse, G.; Furthmüller, J. *Comput. Mat. Sci.* **1996**, *6*, 15.

5) Kresse, G.; Furthmüller, J. *Phys. Rev. B* **1996**, *54,* 11169.

6) Blochl, P. E. *Phys. Rev. B* **1994**, *50*, 17953.

7) Kresse, G.; Joubert, D. *Phys. Rev. B* **1999**, *59,* 1758.

8) Perdew, J. P.; Burke, K.; Ernzerhof, M. *Phys. Rev. Lett.* **1996**, *77,* 3865.

9) Henkelman, G.; Uberuaga, B. P.; Jónsson, H. *J. Chem. Phys.* **2000**, *113,* 9901.

10) Henkelman, G.; Jónsson, H. *J. Chem. Phys.* **2000**, *113,* 9978.

11) Luo, X.; Sullivan, M. B.; Quek, S. Y. *Phys. Rev. B* **2012**, *86*, 184111.

12) Cheng, L.; Liu, H. J.; Zhang, J.; Wei, J.; Liang, J. H.; Shi, J.; Tang, X. F. *Phys. Rev. B* **2014**, *90*, 085118.

13) Klimeš, J.; Bowler, D. R.; Michaelides, A. *Phys. Rev. B* **2011**, *83*, 195131.

14) Li, Y.Y.; Wang, G.; Zhu, X.-G.; Liu, M.-H.; Ye, C.; Chen, X.; Wang, Y.-Y.; He, K.; Wang, L.-L.; Ma, X.-C.; Zhang, H.-J.; Dai, X.; Fang, Z.; Xie, X.-C.; Liu, Y.; Qi, X.-L.; Jia, J.-F.; Zhang, S.-C.; Xue, Q.-K. *Adv. Mater.* **2010**, *22*, 4002.

15) Liu, Y.; Bian, G.; Miller, T.; Bissen, M.; Chiang, T.-C. *Phys. Rev. B* **2012**, *85*, 195442.

16) Liu, Y.; Wang, H.-H.; Bian, G.; Zhang, Z.; Lee, S. S.; Fenter, P. A.; Tischler, J. Z.; Hong, H.; Chiang, T.-C. Phys. Rev. Lett. **2013**, *110*, 226103.

17) Maassena, J.; Lundstrom, M. *Appl. Phys. Lett.* **2013**, *102*, 093103.

18) Liu, W.; Peng, X.; Wei, X.; Yang, H.; Stocks, M.; Zhong, J. *Phys. Rev. B* **2013**, *87*, 205315.

19) Saeed, Y.; Singh, N.; Schwingenschlögl. U. *Appl. Phys. Lett.* **2014**, *104*, 033105.

20) Feibelman, P. J. *Phys. Rev. Lett.* **1990**, *65*, 729.

21) G. Farin, *Curves and surfaces for computer aided geometric design: A practical guide*, 4th ed. (Academic Press, San Diego, 1997).